

ARTICLE OPEN



High-precision in situ 3D ultrasonic imaging of localized corrosion-induced material morphological changes

Yunda Chen¹, Zirui Yang¹, Xinru Bai¹, Fangxin Zou¹✉ and Frederic B. Cegla²

We present an ultrasonic research technique that can carry out in situ, direct monitoring of the 3D morphologies of corrosion substrates. The technique has a customizable lateral resolution, an ultra-high axial resolution of 100 nm, and an experimentally proven measurement accuracy. In using the technique to monitor the localized corrosion processes of carbon steel under constant DCs, it was observed that during each of the experiments conducted in alkaline environments, iron dissolution accelerated for a certain period of time and then slowed down. Based on the various features of the ultrasonic signals acquired and the XRD spectra of the corrosion products obtained, it was deduced that an increase in iron dissolution rate as such was accompanied by the depositing of solid corrosion products onto the substrate used and driven by the formation of Fe_3O_4 , which consumed electrons. After a while, the corrosion product layer collapsed and the formation of Fe_3O_4 was halted.

npj Materials Degradation (2023)7:77; <https://doi.org/10.1038/s41529-023-00395-w>

INTRODUCTION

Steel corrosion is one of the main causes of structural degradation and failure in many areas, e.g., marine infrastructure, petrochemical plants, automobiles, etc. According to the IMPACT study conducted by NACE International, the global cost of corrosion in 2013 was approximately US\$2.5 trillion, equivalent to 3.4% of the global GDP¹. Since a corrosion system would inevitably embody certain non-uniformity, e.g., unevenness in the surface and the composition of the electrode, spatial variations in the contents of the electrolyte solution, etc., localized corrosion, which would cause the different areas of an electrode to dissolve at different rates, often takes place. Compared with uniform corrosion, localized corrosion is much more difficult to predict and detect, and routinely leads to rapid deteriorations of structural integrity and pre-mature structural failures². In order to enable the designing of safer structures against localized corrosion, much effort has been devoted to understanding the kinetics of localized corrosion^{3–8}.

Localized corrosion essentially leads to 3D morphological changes that evolve with time. Therefore, an intuitive approach to studying the kinetics of localized corrosion would be to conduct in situ 3D monitoring of the morphologies of corrosion substrates during localized corrosion experiments. A number of in situ microscopic techniques that are derived from STM^{9–12}, AFM^{13,14}, confocal laser scanning microscopy^{15,16}, optical microscopy¹⁷, etc. have been used to obtain direct observations of the morphological evolution processes of corrosion substrates. However, these techniques are not able to “see” through corrosion product layers, making them inapplicable in many real-life corrosion systems. In situ X-ray computed tomography (XCT) has shown considerable superiority in monitoring the morphologies of corrosion substrates^{18,19}. However, the technique suffers from two major limitations: first, the X-rays employed are high-energy^{20,21} and therefore could impact the kinetics of corrosion reactions; more importantly, a single XCT measurement can take up to 10 s of minutes to complete^{22,23}, rendering the technique incapable of capturing transient corrosion phenomena. Another class of

techniques for realizing in situ 3D monitoring of the morphologies of corrosion substrates rely on acquiring the localized electrochemical properties of a substrate and converting the electrochemical information into morphological information based on certain empirical relationships. In this case, in situ electrochemical measurements are usually made by manipulating one of the electrodes of the corrosion system. For instance, a working electrode can be discretized into an array of electrically insulated wire beams, whose electrochemical properties are acquired individually^{24,25}. However, in using a wire beam electrode, any discrepancy between the initial surface morphologies of the different beams would limit measurement accuracy²⁶, and the fact that the working electrode is made up of several electrically insulated pieces could distort the corrosion process. Scanning electrochemical microscopy techniques, such as the scanning reference electrode technique and the scanning vibrating electrode technique^{27–31}, instead make use of a moveable reference electrode to acquire the electrochemical properties of the different micro-sections of a working electrode. However, these techniques lack the ability to differentiate between Faradaic currents, which are induced by metal dissolution, and non-Faradaic currents, undermining the accuracy of the evaluation of corrosion rates.

To realize more in-depth studies on the kinetics of localized corrosion, a research tool that can monitor the morphologies of corrosion substrates in a direct, non-intrusive, and corrosion product-immune manner would be highly desirable. In our previous works, we introduced an ultrasonic technique that makes use of a single piezoelectric transducer element to monitor uniform corrosion processes^{32–34}. The measurement resolution of the technique reaches 10 s nm and its accuracy was well validated by a number of independent methods. What's more, it was shown that in the context of corrosion monitoring, ultrasound possesses many advantages over other diagnostic means. For instance, the conversion of ultrasonic signal features to morphological information is direct and does not require any assumption. Also, due to its extremely low energy level, ultrasound does not affect the kinetics

¹Department of Aeronautical and Aviation Engineering, The Hong Kong Polytechnic University, Hung Hom, Kowloon, Hong Kong SAR, China. ²Non-Destructive Evaluation Group, Department of Mechanical Engineering, Imperial College London, London SW7 2AZ, UK. ✉email: frank.zou@polyu.edu.hk

of corrosion reactions. Furthermore, since in an experiment ultrasound will be injected from the non-working surface of the corrosion substrate, it will not be impeded by any corrosion product that deposits on the working surface of the substrate. However, the previously introduced technique cannot be used to study localized corrosion because it is only able to monitor the average thickness loss of a relatively large area of a corrosion substrate, lacking in-plane spatial resolution.

In this work, we introduce an ultrasonic technique that is able to monitor localized corrosion processes directly and non-intrusively and “see” through corrosion product layers. To construct a monitoring setup, a 2D multi-element piezoelectric transducer array is permanently attached to the non-working surface of a corrosion substrate. In a localized corrosion experiment, the transducer elements each track the thickness loss of one micro-section of the corrosion substrate. At any moment in time, the morphology of the entire corrosion substrate is obtained by interpolating the thickness losses of all the micro-sections. The lateral resolution of the proposed technique is customizable and related to the dimension of the transducer elements used, the frequency of the ultrasonic waves excited, and the thickness of the corrosion substrate used. Its axial resolution, on the other hand, was found to be as high as 100 nm. The proposed technique was utilized in a number of localized corrosion experiments that were performed using NAK80 steel substrates in a neutral NaCl solution. With the help of white light interferometry, the measurement accuracy of the proposed technique was carefully analyzed.

The proposed technique was further used to observe the corrosion processes of NAK80 steel under different pH levels. By taking into consideration multiple ultrasonic signal features, the proposed technique became capable of revealing simultaneously both the morphological evolution process of a corrosion substrate and the formation and destruction process of the corrosion product layer on the substrate. Such measurement capability, which has not been demonstrated by other techniques, was exploited in this work to carry out some preliminary but original studies on the effect of corrosion products on the kinetics of localized corrosion.

RESULTS AND DISCUSSION

Ultrasonic corrosion monitoring setup

Figure 1a shows the hardware of the proposed ultrasonic technique for monitoring localized corrosion. On one of the surfaces of a corrosion substrate, a 3D-printed corrosion chamber that is linked to an electrolyte reservoir is affixed by silicone rubber. Inside the corrosion chamber, a customized counter electrode that is connected to a DC power supply is embedded. On the non-working surface of the corrosion substrate, a 2D multi-element piezoelectric transducer array (PZT-5H, Kaiqing Optoelectronic Materials, China) is adhered to by epoxy resin. An inhouse robotic arm is employed to allow an arbitrary waveform generator (AWG)/oscilloscope unit (Handyscope HS5, TiePie Engineering, Netherlands) to connect to any of the transducer elements. Next to the transducer array, a resistance temperature detector (RTD) is glued on by thermally conductive epoxy resin. The RTD is connected to a resistance data logger (PT104, Pico Technology, UK).

In an experiment, electrolyte solution is circulated through the corrosion chamber and makes contact with the corrosion substrate. If necessary, the corrosion process can be accelerated by applying a DC across the corrosion substrate and the counter electrode. Meanwhile, the AWG/oscilloscope unit is AC-coupled with the transducer elements in a round-robin manner via the robotic arm, commanding each transducer element to generate an ultrasonic shear wave that propagates in the thickness direction of the corrosion substrate, and acquire the reflection off the working surface. The shear waves generated by the transducer elements

each insonify a finite micro-section of the corrosion substrate. The instantaneous thickness (T_h) of each insonified micro-section is calculated by

$$T_h = \frac{V(T) \cdot (ToA_2 - ToA_1)}{2} \quad (1)$$

where $V(T)$ is the temperature-dependent velocity of the shear wave excited, and ToA_1 and ToA_2 indicate the time-of-arrival's of the first and the second reflected wavepackets in the reflection signal (see “Determination of reflected wavepacket time-of-arrival's” section). After each round of signal generation and acquisition, the instantaneous morphology of the corrosion substrate is reconstructed by interpolating the instantaneous thicknesses of all the insonified micro-sections. Throughout the experiment, the RTD continuously records the temperature of the corrosion substrate in order to facilitate the determination of the velocities of the shear waves excited (see “Determination of shear wave velocities” section).

In this work, the corrosion substrates used were made from NAK80 steel (Daido Steel, Japan)³⁵, whose chemical composition is provided in Table 1. To effectively capture the corrosion-induced morphologies of NAK80 steel, a millimeter-level lateral resolution would be necessary. By simulating the acoustic wavefields generated by piezoelectric elements in NAK80 steel using the Huygens' Principle³⁶ and the finite element method (FEM), it was determined that the piezoelectric transducer arrays and the corrosion substrates should most ideally adopt the configurations shown in Fig. 1b, which would give rise to a lateral resolution of 5 mm × 5 mm and a field of view (FoV) of 30 mm × 30 mm (see Supplementary Information). Generally speaking, the lateral resolution and the FoV of the proposed ultrasonic monitoring technique can be customized by adjusting the number of transducer elements used, the dimension of the transducer elements used, the frequency of the ultrasonic wave excited, and the thickness of the corrosion substrate used.

In order to induce different morphological evolution processes in different localized corrosion experiments, three corrosion cells were employed as shown in Fig. 1c. The first corrosion cell consists of a cylindrical corrosion chamber (substrate/electrolyte contact area: $55^2 \pi$ mm², height: 30 mm) and a carbon bar counter electrode (diameter: 3 mm, immersion length: 25 mm, electrode-to-substrate distance: 5 mm) that is fixed in the center of the corrosion chamber. The second corrosion cell consists of a rectangular corrosion chamber (substrate/electrolyte contact area: 60 × 60 mm², height: 60 mm) and a couple of round copper plate counter electrodes (diameter: 2 mm, pitch: 21 mm, electrode-to-substrate distance: 10 mm) that are positioned around the center of the corrosion chamber along one of the diagonals. The third corrosion cell, which is also made up of a rectangular corrosion chamber (substrate/electrolyte contact area: 50 × 50 mm², height: 15 mm), embodies a copper mesh counter electrode (width: 50 mm, height: 10 mm, electrode-to-substrate distance: 5 mm) that is mounted on one of the sidewalls of the corrosion chamber. Figure 1c displays the normalized current fields that the three corrosion cells would theoretically impose upon corrosion substrates under any applied DC (see “Numerical prediction of morphological evolution processes” section).

Impact of ultrasound on corrosion kinetics

Before conducting the core experiments of this work, additional experiments had been carried out with a view to verify that ultrasound does not affect the kinetics of corrosion reactions (see Supplementary Information).

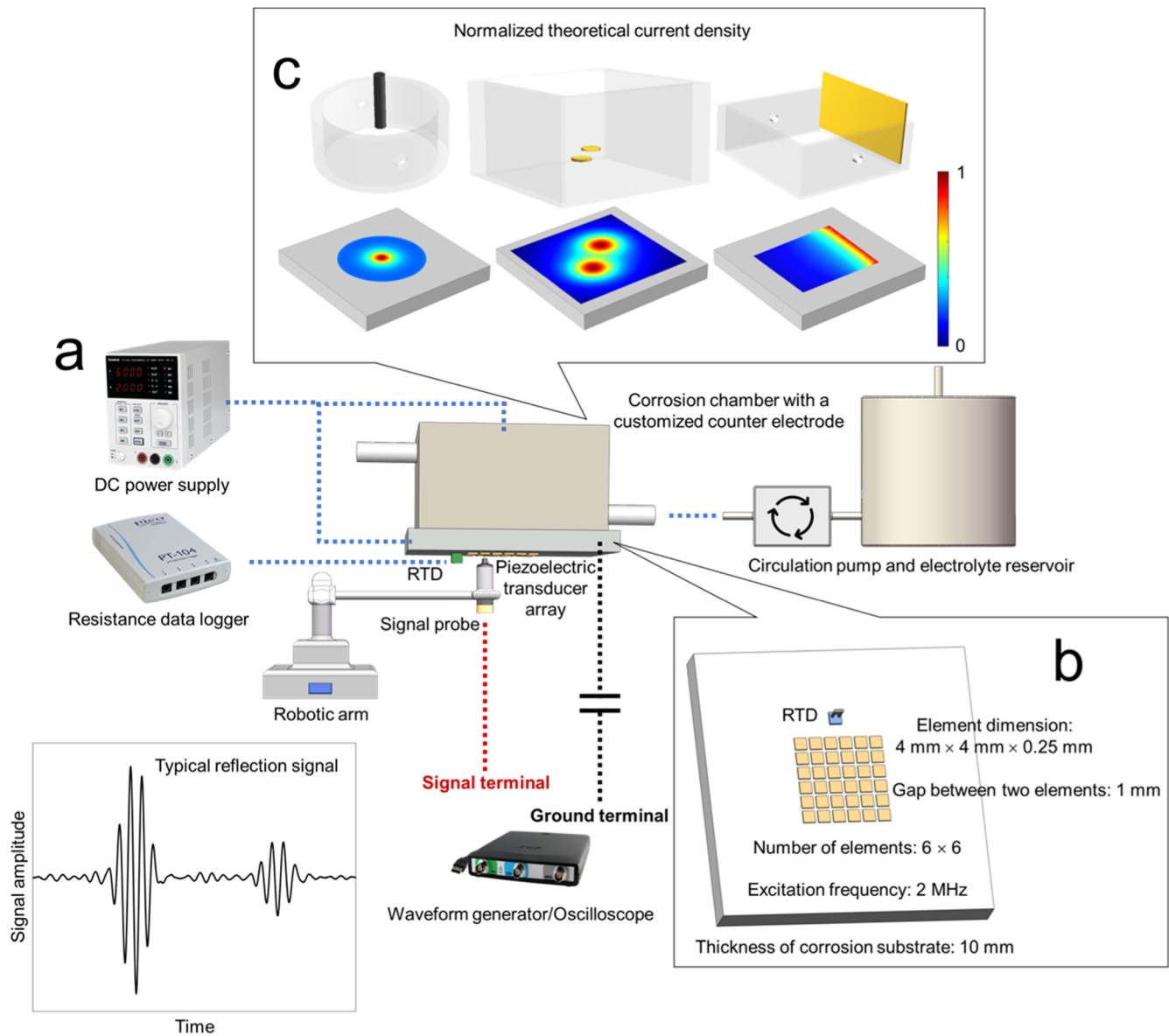


Fig. 1 Overview of the proposed ultrasonic technique for monitoring localized corrosion. **a** A schematic diagram of the hardware. **b** The configurations of the piezoelectric transducer arrays and the corrosion substrates used in this work. **c** The three corrosion cells used in this work and the spatial distributions of the current fields that they would impose upon corrosion substrates.

Table 1. The chemical composition of NAK80 steel.

Element	Fe	C	Si	Ni	Mn	Mo	Cu	Al	Cr
Weight (%)	92.45	0.15	0.3	3	1.5	0.3	1.0	1.0	0.3

Shear wave velocity vs. temperature relationships and axial resolution

Figure 2a and Supplementary Fig. 5 show the shear wave velocity vs. temperature relationships of all the insonified micro-sections of one of the corrosion substrates employed in this work. Expectedly, linearly decreasing trends are observed.

The corrosion substrate retained a constant thickness throughout the experiment for obtaining shear wave velocity vs. temperature relationships. For each insonified micro-section of the corrosion substrate, its thicknesses at different time instants in the 24-hour experiment were also reconstructed from its shear wave velocities at different time instants, and the ToAs of the

reflected wavepackets received at different time instants. As shown in Fig. 2b, if a constant shear wave velocity was used to reconstruct the thicknesses of an insonified micro-section at different time instants, the thickness reconstruction would drift with temperature. On the other hand, if temperature-compensated shear wave velocities were used, the thickness reconstruction would become much more stable. Figure 2c shows the distribution of the standard deviations of the temperature-compensated thickness reconstructions of all the insonified micro-sections of the corrosion substrate. The mean standard deviation, which reflects the axial resolution of the proposed ultrasonic monitoring technique, is 85 nm.

Morphological evolution process monitoring and measurement accuracy

Four localized corrosion experiments were conducted using the proposed ultrasonic monitoring technique. The details of the experiments are provided in Table 2. Before each experiment, the

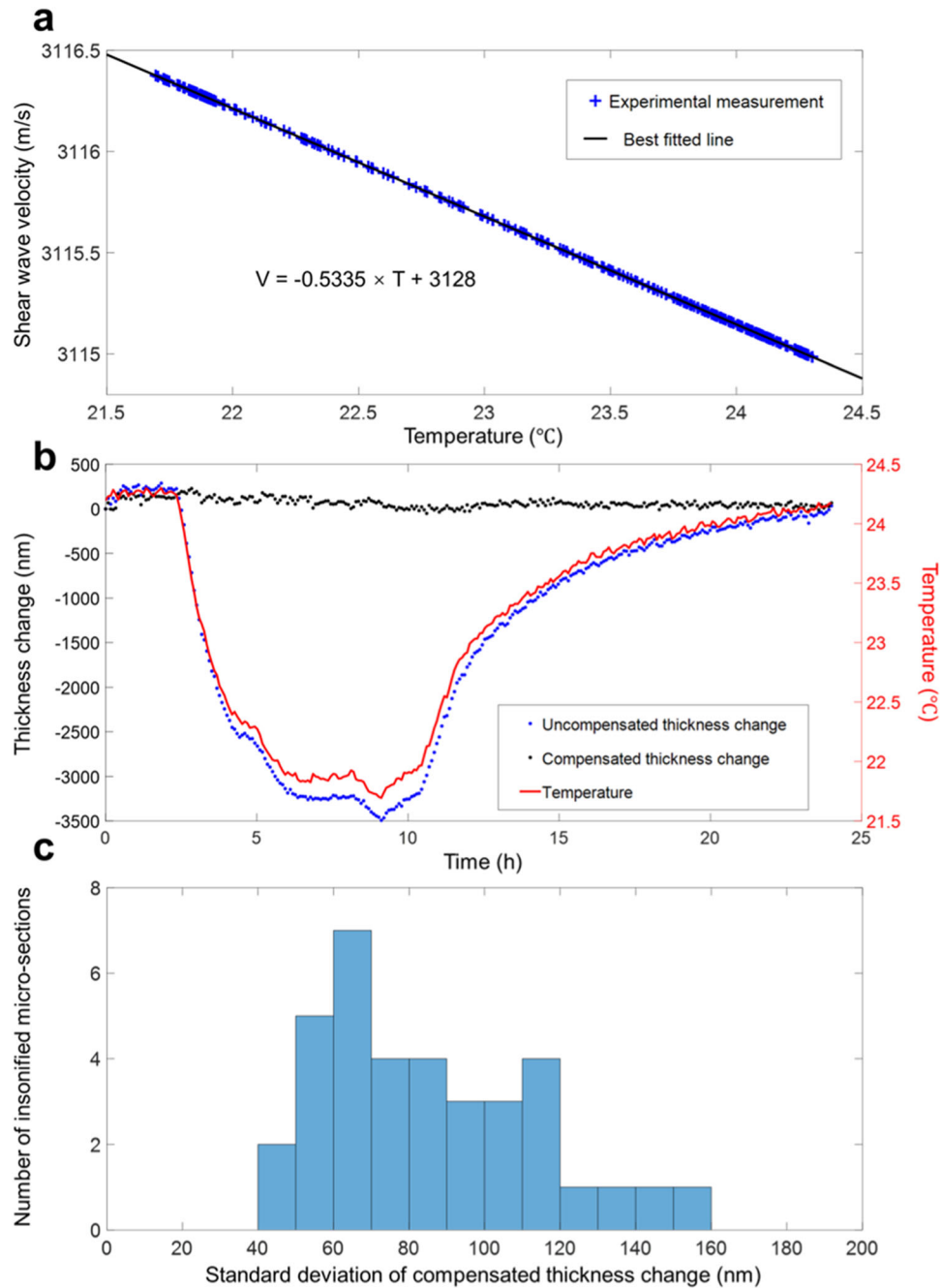


Fig. 2 From attainment of temperature-dependent shear wave velocities to evaluation of the axial resolution of the proposed ultrasonic monitoring technique. **a** The shear wave velocity vs. temperature relationship of one of the insonified micro-sections of one of the corrosion substrates used in this work. **b** The temperature variation of the corrosion substrate and the thickness reconstructions of the aforementioned insonified micro-section. **c** The standard deviations of the temperature-compensated thickness reconstructions of all the insonified micro-sections of the corrosion substrate.

Table 2. The details of the four localized corrosion experiments that were conducted to demonstrate the capability of the proposed ultrasonic monitoring technique.

	Experiment #1	Experiment #2	Experiment #3	Experiment #4
Corrosion substrate ID	CS-1	CS-2	CS-3	CS-4
Electrode	Carbon bar	Copper plates	Copper mesh	
Electrolyte	3.5 wt.% NaCl solution (pH: 7)			3.5 wt.% NaCl + 0.1 M NaOH solution (pH: 13)
Applied DC	50 mA			
Duration	3 hours		6.5 hours	6 hours

working surface of the corrosion substrate was ground and polished using a series of sandpapers with increasing fineness (grit sizes: 80–1500), and then cleaned with deionized water and ethanol. To execute the experiment, 500 mL of electrolyte solution, prepared from deionized water (conductivity: 18.2 M Ω cm @ 25 °C), was added to the electrolyte reservoir and circulated through the corrosion chamber. After the experiment, the working surface of the corrosion substrate was flushed by deionized water.

The morphological evolution processes that would occur under different applied DCs and different durations were predicted numerically (see “Numerical prediction of morphological evolution processes” section). The applied DCs and durations used in Experiments #1, #2, and #3 were determined based on the consideration that the three experiments would induce comparable minimum thickness losses within the FoVs of the transducer arrays. For each of these three experiments, the working surface of the corrosion substrate was scanned by an ex-situ 3D optical profiler (Nexview, Zygo, USA) both before the corrosion process had taken place and after the corrosion products had been washed away. By taking the difference between the two optical scans, an optical measurement of the end-state morphological change of the corrosion substrate was obtained.

In Fig. 3a, e, i, the ultrasonic reconstructions of the morphological evolution processes of the corrosion substrates CS-1, CS-2, and CS-3 are compared to the numerical predictions. While the general trends of the two types of data are in very good agreement, it can be inferred that the actual morphological changes, which should be more closely reflected by the ultrasonic reconstructions, were always more severe than the idealized scenarios, implying that the actual corrosion processes would have been more complex than simple iron dissolution (see “Impact of corrosion products on morphological evolution processes” section).

In Fig. 3b, f, j, the ultrasonic reconstructions of the end-state morphological changes of CS-1, CS-2, and CS-3 are benchmarked against the optical measurements. As demonstrated by the cross-sectional views in Fig. 3c, g, k, the two types of measurement results, attained by different techniques, match reasonably well with each other, except at locations where the gradient of the surface is steep. The mismatches can be attributed to the fact that a non-flat surface will cause the waveform and the propagation path of the reflected wave to deviate from those of the incoming wave^{37,38}.

Figure 3d, h, l compare, micro-section by micro-section, the ultrasonic reconstructions, the optical measurements, and the numerical predictions of the end-state morphological changes of CS-1, CS-2, and CS-3. Note that for each micro-section, the ultrasonic reconstruction is presented as a single-value thickness loss that was determined based on the ultrasonic signals acquired, whereas the optical measurement and the numerical prediction were each obtained by averaging over the optically measured or the numerically predicted thickness losses of all the points within the micro-section (see Supplementary Fig. 6 for the ultrasonic reconstruction and the numerical prediction of the thickness evolution process of each micro-section). Both the ultrasonic reconstructions and the optical measurements, which should closely resemble the actual morphological changes, suggest greater thickness losses than the numerical predictions do, further hinting at the complexity of the actual corrosion processes. The mean difference between the ultrasonic reconstructions and the optical measurements is 6.77%.

Figure 4a illustrates the ultrasonic reconstruction of the morphological evolution process of the corrosion substrate CS-4 (see Supplementary Fig. 7 for the ultrasonic reconstructions of the thickness evolution processes of all theinsonified micro-sections). As observed in Fig. 4b, after Experiment #4, a dark corrosion

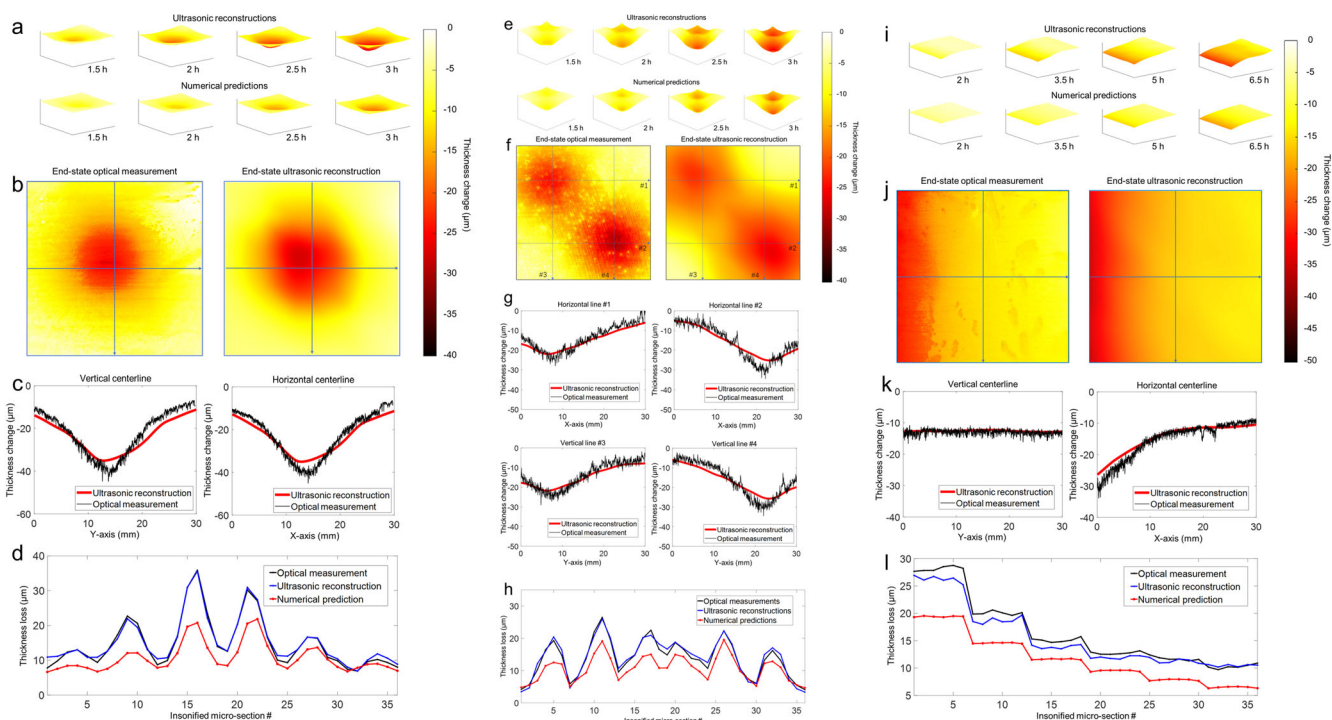


Fig. 3 Results from Experiments #1, #2, and #3. The ultrasonic reconstructions and the numerical predictions of the morphological evolution processes of **a** CS-1, **e** CS-2, and **i** CS-3. The ultrasonic reconstructions and the optical measurements of the end-state morphological changes of **b** CS-1, **f** CS-2, and **j** CS-3. The ultrasonic reconstructions and the optical measurements of the end-state cross-sections of **c** CS-1, **g** CS-2, and **k** CS-3. The ultrasonic reconstructions, the optical measurements, and the numerical predictions of the end-state thickness losses of **d** CS-1, **h** CS-2, and **l** CS-3.

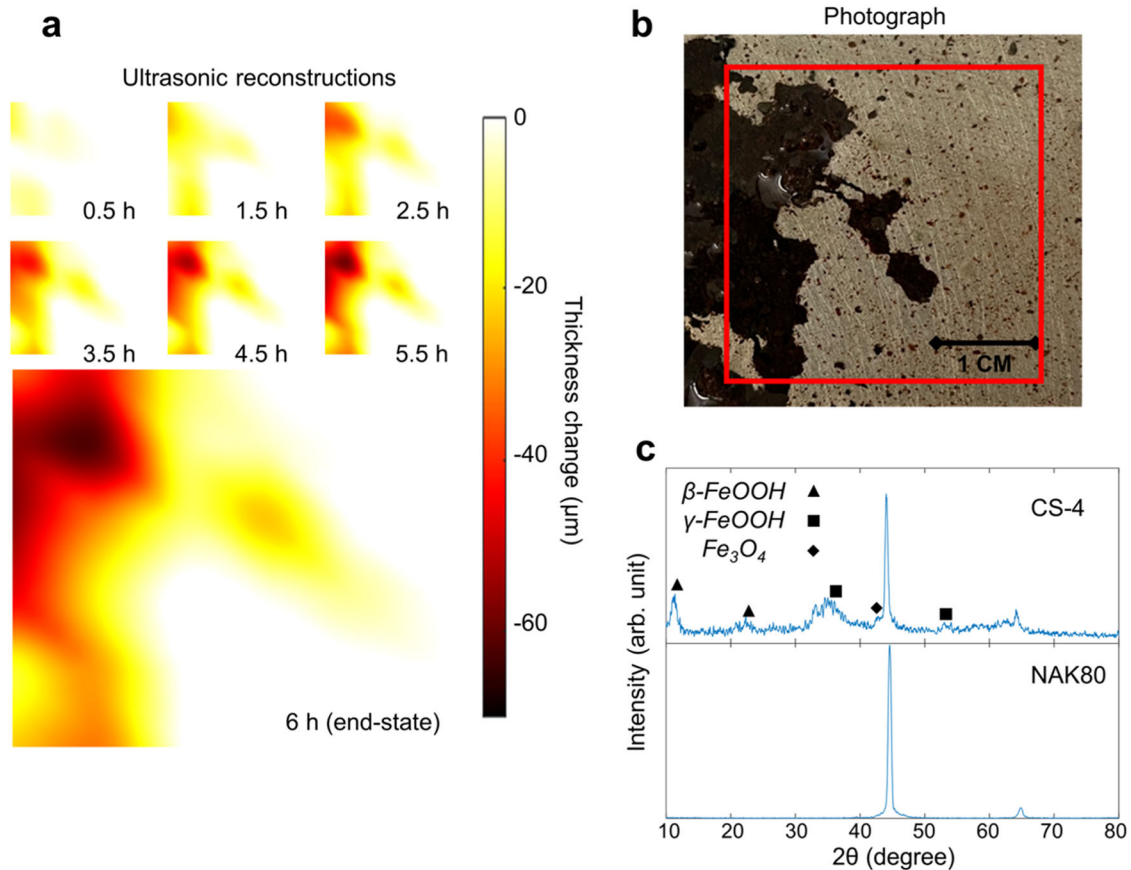


Fig. 4 Results from Experiment #4. **a** The ultrasonic reconstruction of the morphological evolution process of CS-4. **b** A photograph of the end-state morphological change of CS-4 (red rectangle: the FoV of the transducer array). **c** The XRD spectrum of the corrosion products on CS-4 and that of raw NAK80 steel.

product layer, which could not be flushed away by deionized water, remained firmly attached to the working surface of CS-4. The corrosion products were analyzed by XRD (SmartLab SE, Rigaku, Japan) and found to be typical corrosion-induced iron oxides, as shown in Fig. 4c. Owing to the presence of the corrosion product layer, a 3D optical measurement of the end-state morphological change of CS-4 could not be obtained. However, by comparing Fig. 4a, b, it can be seen that the ultrasonic reconstruction of the end-state morphological change agrees very well with the actual end-state morphological change, at least in the in-plane directions.

CS-3 and CS-4 were subjected to the same applied current field (i.e., the same counter electrode and the same applied DC). However, the morphological change of CS-4 was much more localized, concentrated mainly in the high-current-density region. The highly localized nature of the corrosion process of CS-4 can be understood as follows. First of all, the corrosion resistance of a steel substrate will be higher in an alkaline environment than in a neutral environment. Since initiating corrosion under a higher corrosion resistance will require a higher current density and/or a longer time³⁹, within the duration of Experiment #4, the corrosion initiation process of much of the low-current-density region of CS-4 would not have been completed. Furthermore, when a steel substrate corrodes, the corrosion products that are generated at a certain corrosion site could cause the corrosion resistance of the surrounding material to decrease^{40,41}. Specifically speaking, β-FeOOH and γ-FeOOH could break down the passive film on the surrounding material and Fe₃O₄ could increase the electrical conductivity of the surrounding material. Compared with

Experiment #3, Experiment #4, owing to its alkaline nature and as suggested by Fig. 4c, would have generated much more β-FeOOH, γ-FeOOH, and Fe₃O₄ at every corrosion site. As a result, the high-current-density region of CS-4 would have possessed a significantly higher tendency to corrode.

Impact of corrosion products on morphological evolution processes

The results of Experiments #1, #2, and #3 indicate that the actual morphological changes of the corrosion substrates were more severe than the numerical predictions. To understand the possible mechanism behind this observation, Experiment #3 was repeated using a different corrosion substrate (experiment ID: Experiment #3R, corrosion substrate ID: CS-3R), and the corrosion rates of all the insonified micro-sections of CS-3R were extracted from the corresponding real-time ultrasonic thickness loss measurements which are presented in Supplementary Fig. 8a. The insonified micro-sections of CS-3R are numbered according to the layout shown in Fig. 5a, whereby the ones next to the counter electrode are numbered #1 to #6 and those at the other end #31 to #36. For each insonified micro-section, while its numerically predicted corrosion rate is constant, its actual corrosion rate exhibited a transient surge, as demonstrated in Fig. 5b. What's more, the closer to the working electrode an insonified micro-section is, the earlier in time the transient surge in its corrosion rate took place. It is worth mentioning that the fluctuation in corrosion rate that occurred at the beginning of the experiment can be attributed to the nature of corrosion initiation.

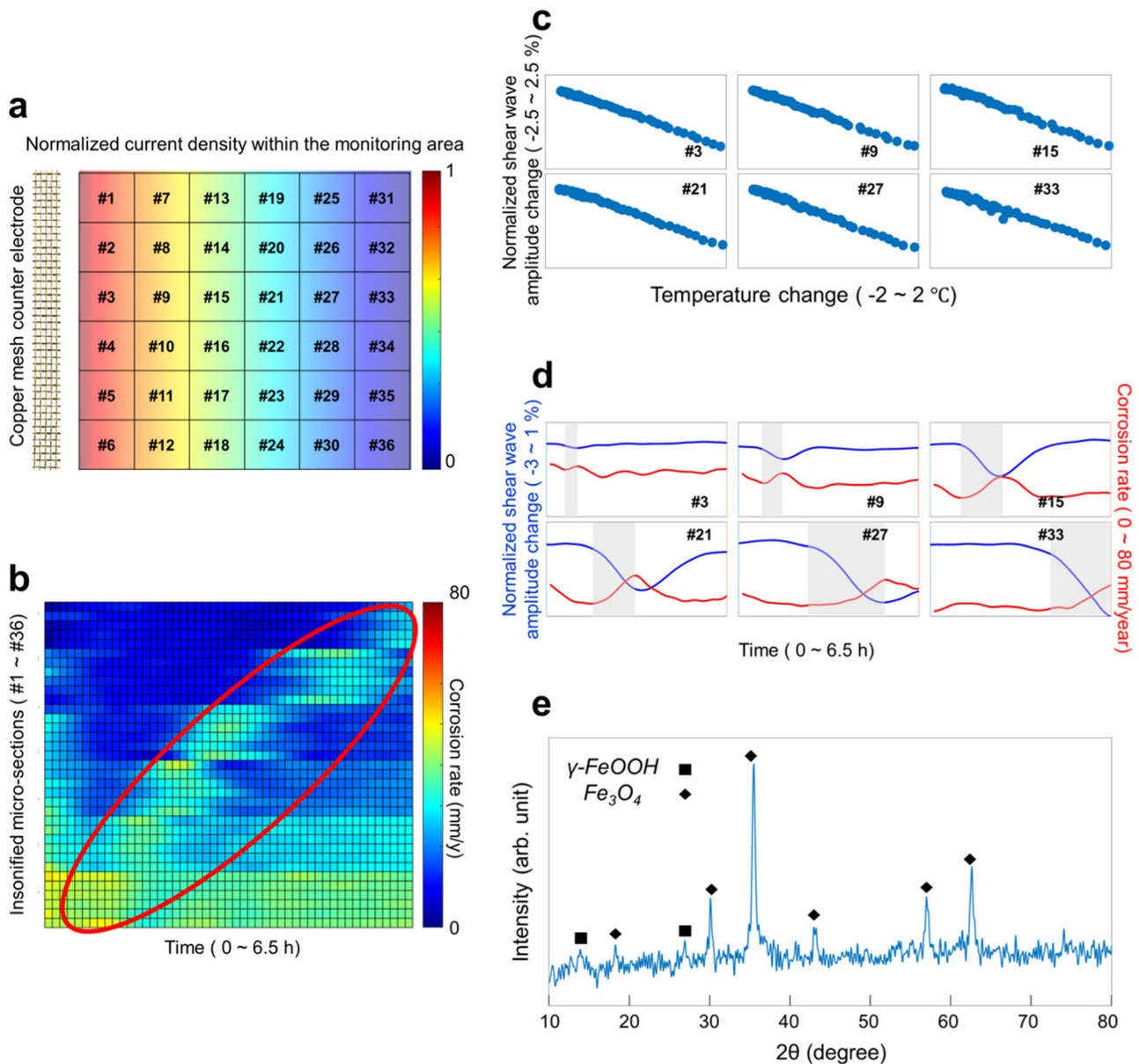


Fig. 5 Results from Experiment #3R. **a** The numbering of the insonified micro-sections of CS-3R. **b** The corrosion rates of all the insonified micro-sections of CS-3R (red ellipse: the transient surges and drops in corrosion rate). **c** The shear wave amplitude vs. temperature relationships of six representative insonified micro-sections of CS-3R. **d** The temperature-compensated peak amplitudes of the first reflected wavepackets that were received at the six representative insonified micro-sections of CS-3R. The corrosion rates of the six representative insonified micro-sections of CS-3R. (Shaded areas: the transient surges in corrosion rate and the transient drops in signal amplitude.) **e** The XRD spectrum of the precipitates in the residual electrolyte solution of Experiment #3R.

Figure 5c and Supplementary Fig. 8b show the shear wave amplitude vs. temperature relationships of all the insonified micro-sections of CS-3R. The data was actually derived from the measurements that were acquired during the experiment for obtaining the micro-section shear wave velocity vs. temperature relationships of CS-3R. For each data point, instead of the velocity of the shear wave excited (as exemplified by Fig. 2a), the peak amplitude of the first reflected wavepacket was plotted.

The micro-section shear wave amplitude vs. temperature relationships of CS-3R were used to compensate for the effect of temperature on the peak amplitudes of the first reflected wavepackets that were received at all the insonified micro-sections of CS-3R throughout Experiment #3R. The results are

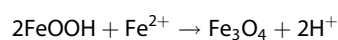
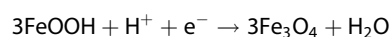
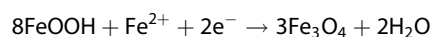
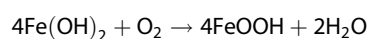
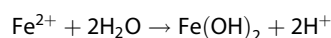
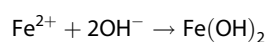
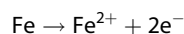
plotted in Fig. 5d and Supplementary Fig. 8c, together with the corrosion rates of all the insonified micro-sections of CS-3R. For each insonified micro-section, the peak amplitudes of the first reflected wavepackets exhibited a transient drop. What's more, the transient drop in signal amplitude coincided in time with the transient surge in corrosion rate. Since shear waves can only propagate in solids, the transient drops in signal amplitude across CS-3R could be attributed to the depositing of a solid corrosion product layer on working surface of CS-3R.

After Experiment #3R had finished, the precipitates in the residual electrolyte solution were analyzed by XRD, revealing the presence of $\gamma\text{-FeOOH}$ and Fe_3O_4 , as shown in Fig. 5e. It has been widely reported that the formation of $\gamma\text{-FeOOH}$ and Fe_3O_4 follows

Table 3. The details of the two localized corrosion experiments that were conducted to validate the relationship between the transformation of γ -FeOOH to Fe_3O_4 and transient surges in corrosion rate.

	Experiment #5	Experiment #6
Corrosion substrate ID	CS-5	CS-6
Electrode	Copper mesh	
Electrolyte	3.5 wt.% NaCl + 0.1 M HCl solution (pH: 1)	3.5 wt.% NaCl + 0.001 M HCl solution (pH: 3)
Applied DC	50 mA	
Duration	6 hours	

the below-mentioned reactions^{40,42–55}:



The high Cl^- concentration of the corrosion environment in Experiment #3R is conducive to the formation of metastable γ -FeOOH^{50,51}. The metastable γ -FeOOH formed would have tended to transform to the stabler Fe_3O_4 ^{48,49,53,54}. The transformation of γ -FeOOH to Fe_3O_4 is an electron-consuming process. Therefore, the actual dissolution rate of CS-3R would have had to be higher than what the applied current field could lead to, in order to supply the electrons needed to generate Fe_3O_4 .

From the abovementioned reactions, it can be seen that the formation of $\text{Fe}(\text{OH})_2$, which is key to generating γ -FeOOH and Fe_3O_4 , depends highly on OH^- concentration. A highly acidic corrosion environment will slow down or even stop the formation of Fe_3O_4 , because the H^+ in the environment will neutralize the OH^- produced by the cathodic reactions. To further validate the relationship between the transformation of γ -FeOOH to Fe_3O_4 and the transient surges in the micro-section corrosion rates of CS-3R, two additional experiments were conducted under different acidities, as detailed in Table 3. The real-time ultrasonic thickness loss measurements of all the insonified micro-sections of the corrosion substrates CS-5 and CS-6 are presented in Supplementary Figs. 9a and 10a. The numbering of the insonified micro-sections also follows the layout shown in Fig. 5a.

As seen from Fig. 6a, b and Supplementary Fig. 9b, none of the insonified micro-sections of CS-5 exhibited any noticeable transient surge in corrosion rate or transient drop in signal amplitude. At the end of Experiment #5, the residual electrolyte solution was found to be clear and free from precipitates. The pH level of the residual electrolyte solution was measured to be 1.3. The continuous high acidity of the corrosion environment would have effectively restrained the formation of $\text{Fe}(\text{OH})_2$ and the subsequent phase transformations. The morphological evolution process of CS-5 was essentially still governed by the applied current field.

The insonified micro-sections of CS-6, on the other hand, exhibited both transient surges in corrosion rate and transient drops in signal amplitude, as shown in Fig. 6b, d and

Supplementary Fig. 10b. Moreover, the XRD spectrum provided in Fig. 6e signifies that γ -FeOOH and Fe_3O_4 were present in the residual electrolyte solution of Experiment #6. By the end of the experiment, the pH level of the electrolyte solution increased to as high as 8.1 because the initial condition of the electrolyte solution was only weakly acidic. Therefore, the formation of γ -FeOOH and Fe_3O_4 can be attributed to the increase in alkalinity of the corrosion environment which would have promoted the formation of $\text{Fe}(\text{OH})_2$.

Based on the experimental results and discussion presented above, the corrosion process of carbon steel in an alkaline environment under a constant applied current field can be understood as follow. As suggested by Figs. 5d and 6d, the corrosion process can be partitioned into three key stages according to the instantaneous corrosion rates. The first stage will embody corrosion initiation, which may very well lead to a fluctuating corrosion rate, and possibly a period during which the corrosion rate will be relatively stable and largely governed by the applied current field. At the end of the first stage, a solid corrosion product layer will start to grow on the working surface of the substrate, causing the amplitudes of the reflected wavepackets to begin to decrease. The start time of the growth of the solid corrosion product layer will decrease with the applied current density, since a higher current density will lead to faster iron dissolution and hence more rapid generation of solid corrosion products. In the second stage, the corrosion rate will start to increase and the amplitudes of the reflected wavepackets will continue to decrease. This can be attributed to an acceleration in the transformation of γ -FeOOH to Fe_3O_4 which will speed up iron dissolution and the growth of the solid corrosion product layer. In the final stage, both the corrosion rate and the amplitudes of the reflected wavepackets will gradually return to the steady-state level. The solid corrosion product layer will now be thick enough to hinder the diffusion of dissolved oxygen. As a result, the oxidation of $\text{Fe}(\text{OH})_2$ to FeOOH and the subsequent transformation of γ -FeOOH to Fe_3O_4 will slow down, reducing the demand on the release of electrons by iron dissolution. Meanwhile, the applied current will continuously degrade the adhesion between the solid corrosion product layer and the substrate, causing the solid corrosion product layer to eventually detach from the substrate.

METHODS

Numerical prediction of morphological evolution processes

The point-wise thicknesses of a corrosion substrate at any moment in time in a localized corrosion experiment can be predicted based on the current field on the substrate, Faraday's law of electrolysis, and the anodic reaction $\text{Fe} \rightarrow \text{Fe}^{2+} + 2\text{e}^-$. The current field on the substrate can be computed using the FEM, by considering the applied DC, the configuration of the counter electrode, and the position of the counter electrode relative to the substrate.

Determination of reflected wavepacket time-of-arrival's

The signal-to-noise ratio (SNR) of a reflection signal directly impacts the measurement accuracy of the ToAs of the first two reflected wavepackets. Therefore, three approaches are used to enhance the SNRs of reflection signals. (i) When a transducer element carries out signal generation and acquisition, it does so 100 times, and the 100 consecutively acquired signals is averaged over. (ii) A 5th-order Butterworth bandpass filter with cut-off frequencies of 1.2 MHz and 2.8 MHz is applied to the *averaged* signal. (iii) The *filtered* signal is auto-correlated, and in the *auto-correlation*, the locations of the first two local peaks correspond to the ToAs of the first two reflected wavepackets.

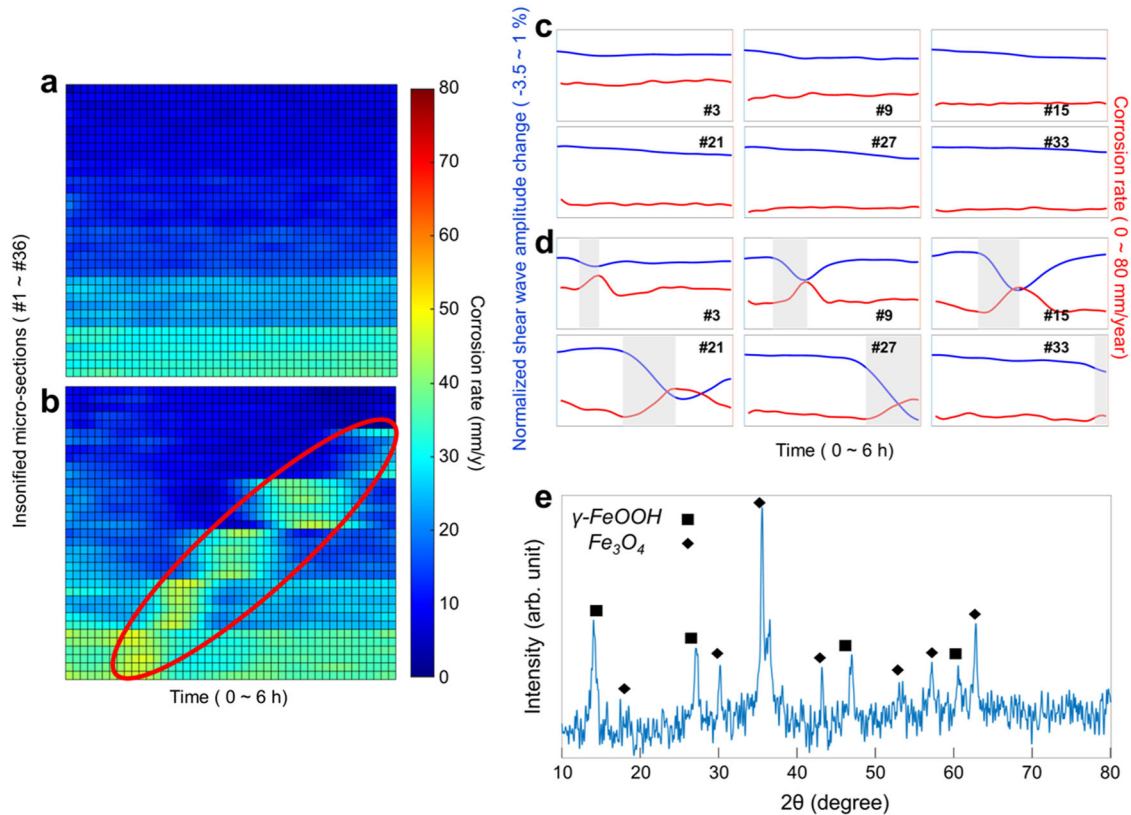


Fig. 6 Results from Experiments #5 and #6. The corrosion rates of **a** all the insonified micro-sections of CS-5 and **b** all the insonified micro-sections of CS-6 (red ellipse: the transient surges and drops in corrosion rate). The temperature-compensated peak amplitudes of the first reflected wavepackets that were received at **c** six representative insonified micro-sections of CS-5 and **d** six representative insonified micro-sections of CS-6. The corrosion rates of **c** the six representative insonified micro-sections of CS-5 and **d** the six representative insonified micro-sections of CS-6. (Shaded areas: the transient surges in corrosion rate and the transient drops in signal amplitude.) **e** The XRD spectrum of the precipitates in the residual electrolyte solution of Experiment #6.

When a reflected wavepacket, which is continuous in nature, is digitized, its *true* ToA could very well be missed out on by sampling points, which are essentially discrete. To minimize the effect of digitization on the measurement accuracy of the ToAs of reflected wavepackets, two tactics are adopted. (i) An *auto-correlation* is up-sampled from 200 MHz to 800 MHz, where 200 MHz is the highest sampling frequency of the AWG/oscilloscope unit used. (ii) As illustrated in Fig. 7, the gradients of the *up-sampled auto-correlation* are calculated at the *apparent* local peak that corresponds to the reflected wavepacket of interest and at an adjacent sampling point; the location of the local zero-gradient point, which resembles more closely the location of the *true* local peak, is determined via linear interpolation, resulting in a more accurate estimate of the ToA of the reflected wavepacket of interest.

Determination of shear wave velocities

The velocity of an ultrasonic wave varies with the temperature of the propagation medium. Therefore, before a corrosion substrate is used for conducting localized corrosion experiments, the shear wave velocity vs. temperature relationships of all the insonified micro-sections of the substrate are evaluated according to the following procedure. (i) The corrosion substrate is exposed to room temperature for 24 hours in the absence of corrosion; the thickness of the substrate remains unchanged; the transducer elements and the RTD on the substrate continuously carry out signal generation and acquisition and temperature measurement respectively, just like what they would do in localized corrosion experiments. (ii) For each insonified micro-section of the corrosion

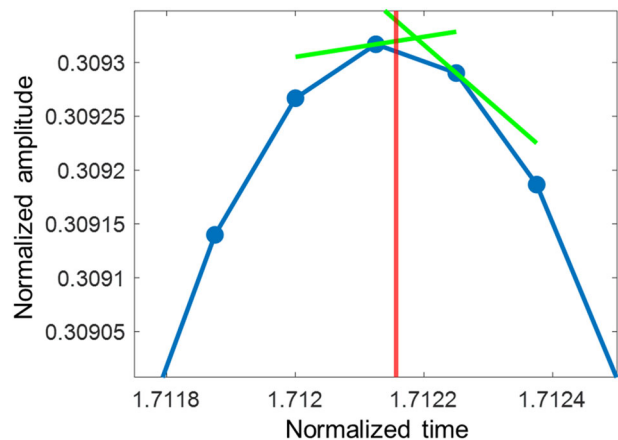


Fig. 7 Gradient-based determination of the exact time-of-arrival of reflected wavepackets. Green lines: the gradients of the up-sampled auto-correlation at an apparent local peak and at an adjacent sampling point, red line: the location of the true local peak.

substrate, the ultrasonic signals acquired in each round of signal generation and acquisition are processed into the ToAs of the first two reflected wavepackets (see “Determination of reflected wavepacket time-of-arrival’s” section). (iii) The ToAs of the first two reflected wavepackets are used to calculate the instantaneous shear wave velocity of the insonified micro-section based on a modified version of Eq. (1), i.e., $V(T) = 2 \cdot Th_i / (ToA_2 - ToA_1)$,

where Th_i is the thickness of the corrosion substrate. (iv) The shear wave velocities of the insonified micro-section at different time instants are plotted against the temperature variation recorded; the shear wave velocity vs. temperature relationship of the insonified micro-section is obtained via linear regression.

In a localized corrosion experiment, the shear wave velocity of an insonified substrate micro-section at a specific time instant is determined based on the temperature recorded at the same time instant, and the pre-determined shear wave velocity vs. temperature relationship of the insonified substrate micro-section.

DATA AVAILABILITY

The datasets generated during and/or analyzed during the current study are available from the corresponding author on reasonable request.

CODE AVAILABILITY

The computer codes supporting the current study are available from the corresponding author upon reasonable request.

Received: 4 May 2023; Accepted: 12 September 2023;

Published online: 27 September 2023

REFERENCES

- Koch, G. et al. International measures of prevention, application, and economics of corrosion technologies study. NACE International, 216 (2016).
- Wood, M. H., Arellano, A. V. & Van Wijk, L. Corrosion related accidents in petroleum refineries. European Commission Joint Research Centre, report no. EUR 26331 (2013).
- Foley, R. Localized corrosion of aluminum alloys—a review. *Corrosion* **42**, 277–288 (1986).
- Frankel, G. Pitting corrosion of metals: a review of the critical factors. *J. Electrochem. Soc.* **145**, 2186 (1998).
- Ryan, M. P., Williams, D. E., Chater, R. J., Hutton, B. M. & McPhail, D. S. Why stainless steel corrodes. *Nature* **415**, 770–774 (2002).
- Ghali, E., Dietzel, W. & Kainer, K.-U. General and localized corrosion of magnesium alloys: a critical review. *J. Mater. Eng. Perform.* **13**, 7–23 (2004).
- Frankel, G. & Sridhar, N. Understanding localized corrosion. *Mater. Today* **11**, 38–44 (2008).
- Tian, W., Li, S., Du, N., Chen, S. & Wu, Q. Effects of applied potential on stable pitting of 304 stainless steel. *Corros. Sci.* **93**, 242–255 (2015).
- Binnig, G. & Rohrer, H. Scanning tunneling microscopy. *Surf. Sci.* **126**, 236–244 (1983).
- Bhardwaj, R., González-Martín, A. & Bockris, J. M. In situ scanning tunneling microscopy studies on passivation of polycrystalline iron in borate buffer. *J. Electrochem. Soc.* **138**, 1901 (1991).
- Kunze, J., Maurice, V., Klein, L. H., Strehblow, H.-H. & Marcus, P. In situ STM study of the effect of chlorides on the initial stages of anodic oxidation of Cu (111) in alkaline solutions. *Electrochim. Acta* **48**, 1157–1167 (2003).
- Massoud, T., Maurice, V., Klein, L. H. & Marcus, P. Nanoscale morphology and atomic structure of passive films on stainless steel. *J. Electrochem. Soc.* **160**, C232–C238 (2013).
- Park, J., Paik, C., Huang, Y. & Alkire, R. Influence of Fe-Rich intermetallic inclusions on pit initiation on aluminum alloys in aerated NaCl. *J. Electrochem. Soc.* **146**, 517 (1999).
- Davoodi, A., Pan, J., Leygraf, C. & Norgren, S. In situ investigation of localized corrosion of aluminum alloys in chloride solution using integrated EC-AFM/SECM techniques. *Electrochem. Solid-State Lett.* **8**, B21 (2005).
- Ilevbare, G., Schneider, O., Kelly, R. & Scully, J. In situ confocal laser scanning microscopy of AA 2024-T3 corrosion metrology: I. Localized corrosion of particles. *J. Electrochem. Soc.* **151**, B453 (2004).
- Schneider, O., Ilevbare, G., Scully, J. & Kelly, R. In situ confocal laser scanning microscopy of AA 2024-T3 corrosion metrology: II. Trench formation around particles. *J. Electrochem. Soc.* **151**, B465 (2004).
- Sullivan, J., Mehraban, S. & Elvins, J. In situ monitoring of the microstructural corrosion mechanisms of zinc–magnesium–aluminium alloys using time lapse microscopy. *Corros. Sci.* **53**, 2208–2215 (2011).
- Michel, A., Pease, B. J., Geiker, M. R., Stang, H. & Olesen, J. F. Monitoring reinforcement corrosion and corrosion-induced cracking using non-destructive x-ray attenuation measurements. *Cem. Concr. Res.* **41**, 1085–1094 (2011).
- Dong, B. et al. Monitoring reinforcement corrosion and corrosion-induced cracking by X-ray microcomputed tomography method. *Cem. Concr. Res.* **100**, 311–321 (2017).
- Sindelar, R., Lam, P., Louthan, M. Jr & Iyer, N. Corrosion of metals and alloys in high radiation fields. *Mater. Charact.* **43**, 147–157 (1999).
- Riazi, H., Danaee, I. & Peykari, M. Influence of ultraviolet light irradiation on the corrosion behavior of carbon steel AISI 1015. *Met. Mater. Int.* **19**, 217–224 (2013).
- Örnek, C. et al. Time-dependent in situ measurement of atmospheric corrosion rates of duplex stainless steel wires. *npj Mater. Degrad.* **2**, 1–15 (2018).
- Noell, P. J., Schindelholz, E. J. & Melia, M. A. Revealing the growth kinetics of atmospheric corrosion pitting in aluminum via in situ microtomography. *npj Mater. Degrad.* **4**, 1–10 (2020).
- Jun, T. Y. The effects of inhomogeneity in organic coatings on electrochemical measurements using a wire beam electrode: Part I. *Prog. Org. Coat.* **19**, 89–94 (1991).
- Wang, M., Tan, M. Y., Zhu, Y., Huang, Y. & Xu, Y. Probing top-of-the-line corrosion using coupled multi-electrode array in conjunction with local electrochemical measurement. *npj Mater. Degrad.* **7**, 16 (2023).
- Yang, L. & Sridhar, N. Coupled multi-electrode array systems and sensors for real-time corrosion monitoring—a review. *CORROSION/2006, paper* (2006).
- Isaacs, H. & Kissel, G. Surface preparation and pit propagation in stainless steels. *J. Electrochem. Soc.* **119**, 1628 (1972).
- Jaffe, L. F. & Nuccitelli, R. An ultrasensitive vibrating probe for measuring steady extracellular currents. *J. Cell Biol.* **63**, 614–628 (1974).
- Lillard, R., Moran, P. & Isaacs, H. A novel method for generating quantitative local electrochemical impedance spectroscopy. *J. Electrochem. Soc.* **139**, 1007 (1992).
- Bayet, E., Huet, F., Keddam, M., Ogle, K. & Takenouti, H. A novel way of measuring local electrochemical impedance using a single vibrating probe. *J. Electrochem. Soc.* **144**, L87 (1997).
- Cui, N., Ma, H., Luo, J. & Chiovelli, S. Use of scanning reference electrode technique for characterizing pitting and general corrosion of carbon steel in neutral media. *Electrochem. Commun.* **3**, 716–721 (2001).
- Zou, F. X. & Cegla, F. B. High accuracy ultrasonic monitoring of electrochemical processes. *Electrochem. Commun.* **82**, 134–138 (2017).
- Zou, F. X. & Cegla, F. B. High-accuracy ultrasonic corrosion rate monitoring. *Corrosion* **74**, 372–382 (2018).
- Zou, F. X. & Cegla, F. B. On quantitative corrosion rate monitoring with ultrasound. *J. Electroanal. Chem.* **812**, 115–121 (2018).
- Daido Steel Co., L. NAK55 NAK80 40 HRC pre-hardened type high performance, high precision plastic mold steel, https://www.daido.co.jp/products/tool/nak80/pdf/en/nak55_80.pdf.
- Wilcox, P., Monkhouse, R., Lowe, M. & Cawley, P. The use of Huygens' principle to model the acoustic field from interdental Lamb wave transducers. (Plenum Press Div Plenum Publishing Corp, 1998).
- Benstock, D., Cegla, F. & Stone, M. The influence of surface roughness on ultrasonic thickness measurements. *J. Acoust. Soc. Am.* **136**, 3028–3039 (2014).
- Howard, R. & Cegla, F. in AIP Conference Proceedings. 050002 (AIP Publishing LLC).
- Bertolini, L., Carsana, M. & Pedferri, P. Corrosion behaviour of steel in concrete in the presence of stray current. *Corros. Sci.* **49**, 1056–1068 (2007).
- Stratmann, M., Bohnenkamp, K. & Engell, H.-J. An electrochemical study of phase-transitions in rust layers. *Corros. Sci.* **23**, 969–985 (1983).
- Dong, Z. H., Shi, W. & Guo, X. P. Initiation and repassivation of pitting corrosion of carbon steel in carbonated concrete pore solution. *Corros. Sci.* **53**, 1322–1330 (2011).
- Evans, U. Mechanism of rusting. *Corros. Sci.* **9**, 813–821 (1969).
- Evans, U. & Taylor, C. Mechanism of atmospheric rusting. *Corros. Sci.* **12**, 227–246 (1972).
- Misawa, T., Hashimoto, K. & Shimodaira, S. The mechanism of formation of iron oxide and oxyhydroxides in aqueous solutions at room temperature. *Corros. Sci.* **14**, 131–149 (1974).
- Pourbaix, M. Atlas of electrochemical equilibria in aqueous solution. *NACE* **307** (1974).
- Stratmann, M. & Hoffmann, K. In situ Mößbauer spectroscopic study of reactions within rust layers. *Corros. Sci.* **29**, 1329–1352 (1989).
- Refaat, P. & Génin, J.-M. The oxidation of ferrous hydroxide in chloride-containing aqueous media and Pourbaix diagrams of green rust one. *Corros. Sci.* **34**, 797–819 (1993).
- Yamashita, M., Miyuki, H., Matsuda, Y., Nagano, H. & Misawa, T. The long term growth of the protective rust layer formed on weathering steel by atmospheric corrosion during a quarter of a century. *Corros. Sci.* **36**, 283–299 (1994).
- Kamimura, T., Hara, S., Miyuki, H., Yamashita, M. & Uchida, H. Composition and protective ability of rust layer formed on weathering steel exposed to various environments. *Corros. Sci.* **48**, 2799–2812 (2006).

50. Rémazeilles, C. & Refait, P. On the formation of β -FeOOH (akaganéite) in chloride-containing environments. *Corros. Sci.* **49**, 844–857 (2007).
51. Ma, Y., Li, Y. & Wang, F. The effect of β -FeOOH on the corrosion behavior of low carbon steel exposed in tropic marine environment. *Mater. Chem. Phys.* **112**, 844–852 (2008).
52. Alizadeh, M. & Bordbar, S. The influence of microstructure on the protective properties of the corrosion product layer generated on the welded API X70 steel in chloride solution. *Corros. Sci.* **70**, 170–179 (2013).
53. Tanaka, H., Mishima, R., Hatanaka, N., Ishikawa, T. & Nakayama, T. Formation of magnetite rust particles by reacting iron powder with artificial α -, β - and γ -FeOOH in aqueous media. *Corros. Sci.* **78**, 384–387 (2014).
54. Dai, N. et al. Effect of the direct current electric field on the initial corrosion of steel in simulated industrial atmospheric environment. *Corros. Sci.* **99**, 295–303 (2015).
55. Ansari, T. Q., Luo, J.-L. & Shi, S.-Q. Modeling the effect of insoluble corrosion products on pitting corrosion kinetics of metals. *npj Mater. Degrad.* **3**, 28 (2019).

ACKNOWLEDGEMENTS

This work is supported by the National Natural Science Foundation of China (Project No.: 52201089), the Department of Science and Technology of Guangdong Province (Project No.: 2021A1515012130), and the Research Grants Council of Hong Kong (Project No.: 25211319). The authors would like to thank the IC Maker Lab of The Hong Kong Polytechnic University for its support in fabricating some of the experimental specimens used in this work.

AUTHOR CONTRIBUTIONS

Y.C.: conceptualization, methodology, software, validation, formal analysis, investigation, resources, data curation, writing—original draft, visualization; Z.Y. and X.B.: investigation, data curation; F.Z.: conceptualization, methodology, formal analysis, resources, writing—review & editing, supervision, project administration, funding acquisition; F.C.: conceptualization, methodology, writing—review & editing.

COMPETING INTERESTS

The authors declare no competing interests.

ADDITIONAL INFORMATION

Supplementary information The online version contains supplementary material available at <https://doi.org/10.1038/s41529-023-00395-w>.

Correspondence and requests for materials should be addressed to Fangxin Zou.

Reprints and permission information is available at <http://www.nature.com/reprints>

Publisher's note Springer Nature remains neutral with regard to jurisdictional claims in published maps and institutional affiliations.



Open Access This article is licensed under a Creative Commons Attribution 4.0 International License, which permits use, sharing, adaptation, distribution and reproduction in any medium or format, as long as you give appropriate credit to the original author(s) and the source, provide a link to the Creative Commons license, and indicate if changes were made. The images or other third party material in this article are included in the article's Creative Commons license, unless indicated otherwise in a credit line to the material. If material is not included in the article's Creative Commons license and your intended use is not permitted by statutory regulation or exceeds the permitted use, you will need to obtain permission directly from the copyright holder. To view a copy of this license, visit <http://creativecommons.org/licenses/by/4.0/>.

© The Author(s) 2023